Superb Li-ion storage of Sn-based anode assisted by conductive hybrid buffering matrix

Jinsil Shin , Sung-Hoon Park * , Jaehyun Hur *

Posted Date: 21 September 2023

doi: 10.20944/preprints202309.1444.v1

Keywords: Sn; hybrid TiO2-C matrix; ternary composite; anode; Li-ion batteries

Article

Superb Li-Ion Storage of Sn-Based Anode Assisted by Conductive Hybrid Buffering Matrix

Jinsil Shin [1], Sung-Hoon Park [2,*] and Jaehyun Hur [1,*]

[1] Department of Chemical and Biological Engineering, Gachon University, 1342 Seongnam-daero, Seongnam 13120, Republic of Korea

[2] Department of Mechanical Engineering, Soongsil University, 369 Sangdo-ro, Dongjakgu, Seoul 06978, Republic of Korea

* Correspondence: should be addressed to Prof. Jaehyun Hur* (jhhur@gachon.ac.kr) and Prof. Sung-Hoon Park* (leopark@ssu.ac.kr).

Abstract: Although Sn has been intensively studied as one of the most promising anode materials to replace commercialized graphite, its cycling performance and rate performance are still unsatisfactory owing to insufficient control of its large volume change during cycling and poor electrochemical kinetics. Herein, we propose a Sn-TiO_2-C ternary composite as a promising anode material to overcome these limitations. The hybrid TiO_2-C matrix synthesized via two-step high-energy ball milling effectively regulated the irreversible lithiation/delithiation of the active Sn electrode and facilitated Li-ion diffusion. At the appropriate C concentration, Sn-TiO_2-C exhibited significantly enhanced cycling performance and rate capability compared to its counterparts (Sn-TiO_2 and Sn-C). Sn-TiO_2-C delivers good reversible specific capacities (669 mAh g^{-1} after 100 cycles at 200 mA g^{-1} and 651 mAh g^{-1} after 500 cycles at 500 mA g^{-1}) and rate performance (446 mAh g^{-1} at 3000 mA g^{-1}). The superiority of Sn-TiO_2-C over Sn-TiO_2 and Sn-C was corroborated by electrochemical impedance spectroscopy, which revealed faster Li-ion diffusion kinetics in the presence of the hybrid TiO_2-C matrix than in the presence of TiO_2 or C alone. Therefore, Sn-TiO_2-C is a potential anode for next-generation Li-ion batteries.

Keywords: Sn; hybrid TiO_2-C matrix; ternary composite; anode; Li-ion batteries

1. Introduction

The need for high-capacity and high-rate Li-ion batteries (LIBs) has been intensified by the growing demand for various applications that require long-lasting and fast-rechargeable batteries, such as portable electric devices and electric vehicles.[1-12] The anode—one of the key components in LIBs—stores or releases energy by hosting/expelling Li ions paired with the cathode. Graphite has been commercialized as a typical anode material owing to its high cycling stability, fast charging, and low self-discharge. However, the low theoretical capacity of graphite (372 mAh g^{-1}) is significant limitation for sustainable use in emerging applications that require high energy density. To resolve this issue, many high-capacity anode materials (e.g., theoretical capacities of 4200 mAh g^{-1} for Si, 2596 mAh g^{-1} for P, 993 mAh g^{-1} for Sn, 1384 mAh g^{-1} for Ge, and 1494 mAh g^{-1} for SnO_2) have been proposed as alternatives to graphite.[13-17]

Sn-based electrodes are excellent candidates for anode materials owing to their high theoretical capacity, low cost, and chemical/mechanical stability. Nevertheless, the practical applications of Sn-based anodes have been hindered by their large volume changes ($Li_{4.4}$ + Sn → $Li_{4.4}Sn$) during lithiation/delithiation, which lead to large capacity loss and degrade the cycling performance.[18] One of the most common strategies for solving this problem is to employ an appropriate secondary component that can buffer the volume expansion of the active material, promoting cycling stability and reversibility. Although this composite approach reduces the overall capacity, the cycling stability can be significantly improved.[19-23] Liu et al. fabricated a spherical-like Sn-Ni alloy composite from SnO_2, NiO, and Super P carbon via annealing at 900 °C for 2 h, which exhibited a reversible capacity of 448.9 mAh g^{-1} with 78.6% capacity retention after 20 cycles.[24] Hassoun et al. studied SnSb-C

Preprints (www.preprints.org) | NOT PEER-REVIEWED | Posted: 21 September 2023 doi:10.20944/preprints202309.1444.v1

nanocomposites prepared using a two-step method (sol-gel and calcination). The electrode exhibited a reversible capacity of 300 mAh g^{-1} at 100 mA g^{-1} after 100 cycles.[25] Youn et al. synthesized N-doped reduced graphene oxide and nanocrystalline tin sulfide composites using a one-step thermal annealing method. The anode exhibited a specific capacity of 562 mAh g^{-1} at 0.2 A g^{-1} after 200 cycles.[26]

Despite these efforts, the cycling performance is still not fully satisfactory, because of the continuous degradation of the specific capacity, which necessitates the development of better composite materials in which the cycling stability is well maintained without significant capacity reduction. Recently, the introduction of an inorganic-carbon hybrid matrix (e.g., TiC-C) to active materials has been demonstrated to be an effective strategy for restraining the volume expansion of active materials.[27-29] This approach exploits the synergistic effect of the binary buffering material, reinforcing the mechanical and electrical properties and outperforming a single-component buffering matrix.

Herein, we propose a ternary composite consisting of Sn-TiO_2-C as a promising Sn-based anode material for high-performance LIBs. Sn-TiO_2-C was prepared via two-step high-energy ball milling (HEBM). The cycling instability of active Sn was better regulated by the TiO_2-C hybrid buffering matrix than by TiO_2 or C alone. This is because of their synergistic buffering role, which is based on the excellent mechanical properties of TiO_2 and high electronic conductivity of C. The superiority of Sn-TiO_2-C to its counterparts (Sn-TiO_2 and Sn-C) with regard to electrochemical performance and kinetics was experimentally confirmed. In addition, the optimal C content (20 wt%) was experimentally determined for the Sn-TiO_2-C electrode. Sn-TiO_2-C exhibited good cycling performance (reversible specific capacity of 691 mAh g^{-1} at 200 mA g^{-1} after 100 cycles) and rate performance (446 mAh g^{-1} at 3 A g^{-1}). Furthermore, the electrochemical reaction mechanism and kinetics of the Sn-TiO_2-C composites were studied.

2. Experimental Section

2.1. Synthesis of Sn-TiO_2-C, Sn-TiO_2, and Sn-C composite

A ternary composite of Sn-TiO_2-C was synthesized using a two-step HEBM process. First, SnO_2 (99.9% trace metal basis, 10 mesh, Sigma–Aldrich) and Ti powder (325 mesh, 99.5% (metal basis), Sigma–Aldrich) were mixed (1:1, mol/mol) and milled at 300 rpm for 30 h in an Ar environment. Then, acetylene black (C) powder (99.9+% S.A. 75 m^2/g, bulk density of 170–230 g L^{-1}, Alfa Aesar) was added to the synthesized material (Sn-TiO_2) at 300 rpm for 30 h. Three different C contents (10, 20, and 30 wt%) were applied to prepare an Sn-TiO_2-C (10, 20, and 30 wt%) electrode. Binary composites of Sn-TiO_2 and Sn-C were synthesized as control samples using one-step HEBM. Sn-TiO_2 was prepared after the first step of HEBM for synthesizing Sn-TiO_2-C, and Sn-C was prepared by milling a mixture of Sn (99.8%, metal basis, Alfa Aesar) and C (8:2, mol/mol) under the same milling conditions used for Sn-TiO_2 preparation. The mechanochemical synthesis routes for Sn-TiO_2-C, Sn-TiO_2, and Sn-C are expressed as follows:

$$\mathrm{Sn}O_2 + \mathrm{Ti} \xrightarrow{1st\ HEBM} Sn + TiO_2 \xrightarrow{2nd\ HEBM\ (+C)} Sn - TiO_2 - C \qquad (1)$$

$$\mathrm{Sn}O_2 + \mathrm{Ti} \xrightarrow{HEBM} Sn - TiO_2 \qquad (2)$$

$$\mathrm{Sn} + \mathrm{C} \xrightarrow{HEBM} \mathrm{Sn} - \mathrm{C}\,. \qquad (3)$$

2.2. Cell preparation

A coin-type cell (CR2032, Rotech, Inc. South Korea) was used to evaluate the electrochemical performance of the anode materials. To prepare the binder solution, polyvinylidene fluoride (average MW 534,000 by GPC, powder, Sigma–Aldrich) was dissolved in anhydrous N-methylpyrrolidone (99.5%, Sigma–Aldrich) for 24 h (12 wt%). A slurry was prepared by dispersing the active material

and conductive C (Super P, 99+%, metal basis, Alfa Aesar) in the binder-dissolved solution such that the weight ratio of the active material, binder, and conductive C was 70:15:15, respectively, followed by stirring at 150 rpm for 24 h. The prepared slurry was casted on Cu foil, followed by the drying in a vacuum oven at 70 °C for 24 h. The dried working electrode was punched into a circular shape (diameter: 1.25 cm). A typical loading amount of electrode material was 1.5 mg. Polyethylene and Li foil (99.9%, metal basis, 0.75 mm thickness, Alfa Aesar) were used as the separator and counter electrode, respectively. Additionally, 1.5 mL of the electrolyte (1 M $LiPF_6$ dissolved in ethylene carbonate/diethylene carbonate, 1:1, v/v) was added during cell assembly. The cells were assembled in an Ar-gas-filled glovebox.

2.3. Characterization

X-ray diffraction (XRD; Rigaku D/MAX-2200, Japan) equipped with Cu-Kα radiation was used to examine the crystalline structures of the samples. High-resolution transmission electron microscopy (HRTEM; JEOL JEM-2100F, Japan) was used to identify the synthesized components of the composite. The morphology of the composite was examined using scanning electron microscopy (SEM; Hitachi SU8600, Japan) at the Smart Materials Research Center for IoT at Gachon University. The elemental distribution was determined via energy-dispersive X-ray spectroscopy (EDS) mapping. X-ray photoelectron spectroscopy (XPS; Thermo Fisher Scientific Alpha XPS system, U.K.) was used to analyze the binding energies of the elements. Calibration was conducted using the C 1s method, in which the binding energy of C 1s was calibrated at 284.6 eV.

2.4. Electrochemical measurement

The voltage profile, rate capability, and cycling performance were measured using a battery cycler (WBCS 3000, WonAtech, South Korea). Cyclic voltammetry (CV; WonAtech ZIVE MP1, Republic of South Korea) and ex situ XRD (Rigaku D/MAX-2200, Japan) were used to analyze the electrochemical reactions during charging and discharging. The Li-ion diffusion kinetics were analyzed using electrochemical impedance spectroscopy (EIS; ZIVE MP1, South Korea) in the frequency range of 1–1000 kHz.

3. Results and Discussion

3.1. Characterization of as-synthesized Sn-TiO_2-C

Figure 1a shows XRD patterns of Sn-TiO_2-C (20 wt%) and Sn-TiO_2. The main 2θ peaks observed at 30.6°, 32.0°, 43.9°, and 44.9° for Sn-TiO_2 corresponded to the (2 0 0), (1 0 1), (2 2 0), and (2 1 1) planes, respectively, of Sn (PDF# 04-0673). The minor peaks observed at 26.6°, 35.9°, 41.2°, and 54.3° (magnified view in **Figure S1**) were assigned to TiO_2 (rutile, PDF# 21-1276). From these results, it is evident that the O atoms were successfully transferred from Sn to Ti ($SnO_2 + Ti \xrightarrow{HEBM} Sn - TiO_2$) via a mechanochemical reaction, during which Sn and TiO_2 nanoparticles (NPs) were homogeneously mixed with a reduced size. Minor peaks corresponding to SnO_2 (cassiterite) were detected, suggesting that some of the SnO_2 (cassiterite) NPs were not completely converted into Sn and TiO_2. This may be associated with the lower standard enthalpy of SnO_2 compared with that of TiO_2.[30, 31] Even when the milling time was increased to 30 h, the SnO_2 was not completely converted into Sn (**Figure S2**). Nevertheless, the coexistence of Sn and SnO_2 in the active material Sn-SnO_2 is not considered detrimental, because the theoretical capacity of SnO_2 is even higher than that of Sn. In addition, Sn and SnO_2 were expected to mix well during HEBM, with a significantly increased surface area relative to the pristine powder state. For Sn-TiO_2-C (20 wt%), although the peaks were broadened relative to Sn-TiO_2 owing to the presence of amorphous C, all the peak positions were identical, indicating that Sn and TiO_2 were only physically mixed with C, without any changes in their chemical properties during the second milling process.

Preprints (www.preprints.org) | NOT PEER-REVIEWED | Posted: 21 September 2023 doi:10.20944/preprints202309.1444.v1

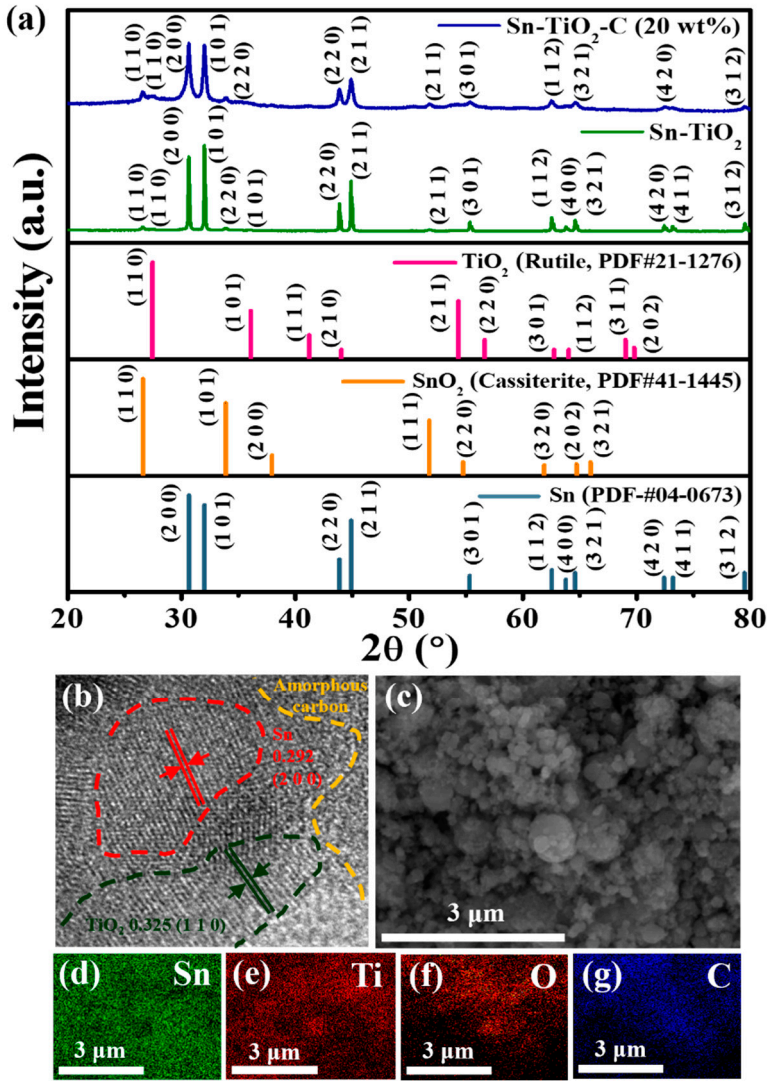

Figure 1. (a) XRD spectra of Sn-TiO_2-C (20 wt%) and Sn-TiO_2 along with theoretical peaks of TiO_2 (rutile, PDF# 21-1276), SnO_2 (cassiterite, PDF# 41-1445), and Sn (PDF# 04-0673). (b) HRTEM and (c) SEM images of Sn-TiO_2-C (20 wt%). (d–g) EDS element maps of Sn-TiO_2-C (20 wt%) for Sn, Ti, C, and O.

The presence and distributions of Sn, TiO_2, and C in the synthesized Sn-TiO_2-C (20 wt%) were characterized using HRTEM, SEM, and EDS. As shown in **Figure 1b**, the presence of Sn (red dotted region, interplanar distance of 0.292 nm from the (2 0 0) plane) and TiO_2 (black dotted region, interplanar distance of 0.325 nm from the (1 1 0) plane) surrounded by amorphous C (orange dotted region) was confirmed in the HRTEM image. Unreacted SnO_2 was also detected, for which the crystallite size was significantly reduced (~5–10 nm) (**Figure S3**) compared with its pristine powder size (~1900 µm according to the vendor). During HEBM, although some SnO_2 particles were not completely converted to Sn and TiO_2, their sizes were significantly reduced, and they were better mixed with the produced Sn and TiO_2, which was beneficial for obtaining high capacity and a stable electrochemical reaction. The average particle size of the as-synthesized Sn-TiO_2-C (20 wt%) was ~305 nm (**Figure S4**), which was far smaller than the sizes of the precursor materials (SnO_2: 1900 µm, Ti: 44 µm) after HEBM. The uniform distributions of constituent atoms (Sn, Ti, C, and O) in the product were confirmed by EDX mapping (**Figures 1c–g**).

Figure 2 shows the XPS spectra of the as-synthesized Sn-TiO_2-C (20 wt%). The survey spectrum confirms the presence of Sn, Ti, O, and C in the sample (**Figure 2a**). In the high-resolution Sn 3d

Preprints (www.preprints.org) | NOT PEER-REVIEWED | Posted: 21 September 2023 doi:10.20944/preprints202309.1444.v1

spectrum, the fitted peaks at 487.2 and 495.6 eV correspond to Sn $3d_{3/2}$ and Sn $3d_{5/2}$, respectively. The peak splitting of 8.4 eV in the Sn 3d spectrum indicates the presence of Sn (**Figure 2b**), which is consistent with the XRD results (**Figure 1a**).[30] The peaks at 464.9 and 459.2 eV with orbital splitting of 5.7 eV in the Ti 2p spectrum correspond to Ti $2p_{1/2}$ and Ti $2p_{3/2}$, respectively, and the presence of TiO_2 in Sn-TiO_2-C (20 wt%) (**Figure 2c**). In the O 1s spectrum, the deconvoluted peaks at 530.4, 531, 532.1, and 533.3 eV correspond to the Ti-O, Sn-O, C-O, and O-H functional groups, respectively (**Figure 2d**). The deconvoluted peaks at 284.6, 286.3, and 289.3 eV in the C 1s spectrum correspond to C-C, C-O-C, and C-O=C, respectively, in Sn-TiO_2-C (20 wt%) (**Figure 2e**). Comparing the XPS spectra of Sn-TiO_2-C (20 wt%) with those of Sn-TiO_2 (**Figure S5**) revealed that most peaks were identical, except for the C 1s spectrum, where the intensities of the C-O-C and C-O=C peaks were significantly reduced owing to the absence of TiO_2-C in Sn-TiO_2.

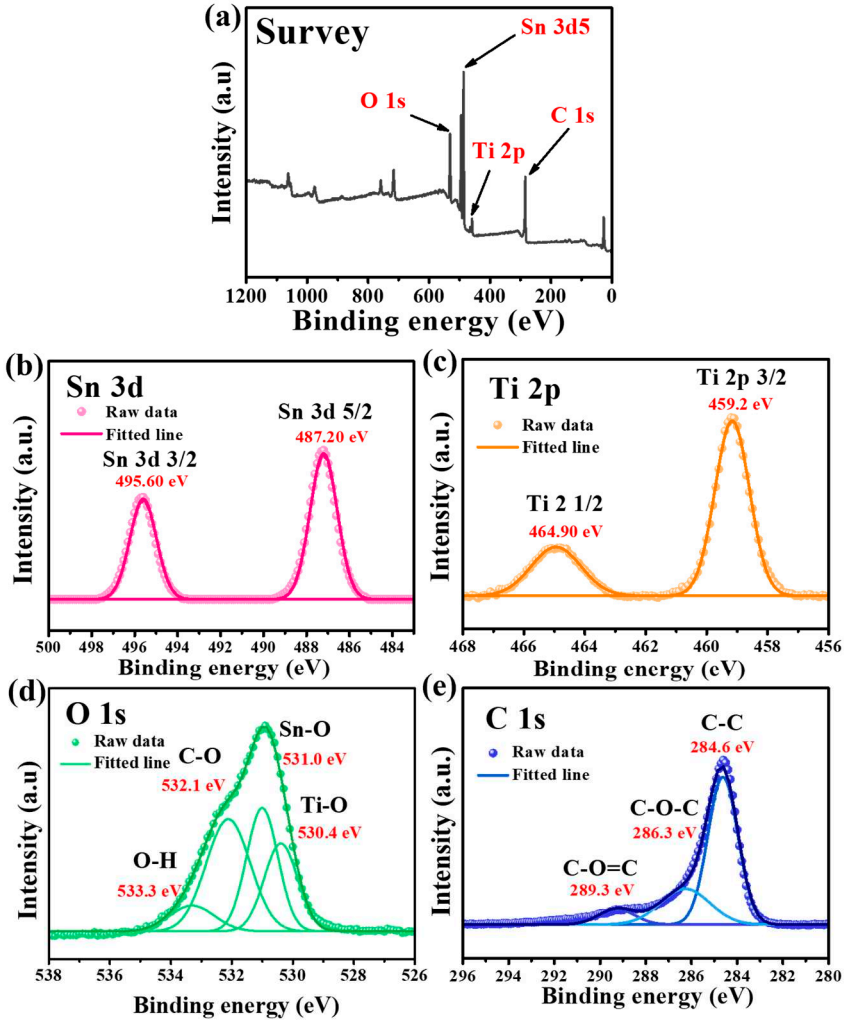

Figure 2. XPS spectra of Sn-TiO_2-C (20 wt%) powder: (a) survey and high-resolution spectra for (b) Sn, (c) Ti, (d) O, and (e) C.

3.2. Electrochemical reaction mechanism and kinetics of Sn-TiO_2-C anode

The electrochemical reaction mechanism of Sn-TiO_2-C (20 wt%) was studied using CV, voltage profiles, and ex situ XRD. **Figure 3a** presents the CV profile of Sn-TiO_2-C (20 wt%) obtained at a voltage scan rate of 0.2 mV s^{-1} for the first five cycles. During the first discharging cycle, three typical lithiation processes of the main active material Sn proceeded at ~0.89 V ($2Li^+ + 2e^- + 5Sn \rightarrow Li_2Sn_5$), ~0.63 V ($31Li^+ + 2Li_2Sn_5 + 31e^- \rightarrow 5Li_7Sn_2$), and ~0.27 V ($9Li^+ + 5Li_7Sn_2 + 9e^- \rightarrow 2Li_{22}Sn_5$). The peak observed at ~1.2 V is attributed to the partial electrolyte decomposition catalyzed by Sn.[12, 31, 32] A broad peak close to ~0 V indicates the lithiation of C and the formation of a solid–electrolyte

Preprints (www.preprints.org) | NOT PEER-REVIEWED | Posted: 21 September 2023 doi:10.20944/preprints202309.1444.v1

interphase (SEI). During the first charge cycle, a series of intermediate products were observed: $Li_{22}Sn_5$, Li_7Sn_3, LiSn, and Li_2Sn_5. The oxidation peak at ~1.2 V is related to the delithiation of Li-C.[33] These electrochemical reactions well match the capacity plateaus in the voltage profile shown in **Figure 3b**. In the ex situ XRD analysis (**Figure 3c**), only $Li_{22}Sn_5$ was detected as the main lithiation product in the fully discharged state. Notably, no other lithiation products were observed, probably because of their small amounts and surface amorphization during lithiation. [34, 35] In the fully charged state, the active Sn peaks clearly reemerged, indicating reversible crystalline evolution of the active material during cycling. After the first cycle, the discharge and charge peaks were broader and smaller, but the peak intensities and positions remained almost unchanged, indicating reversible reactions of Sn-TiO_2-C (20 wt%).

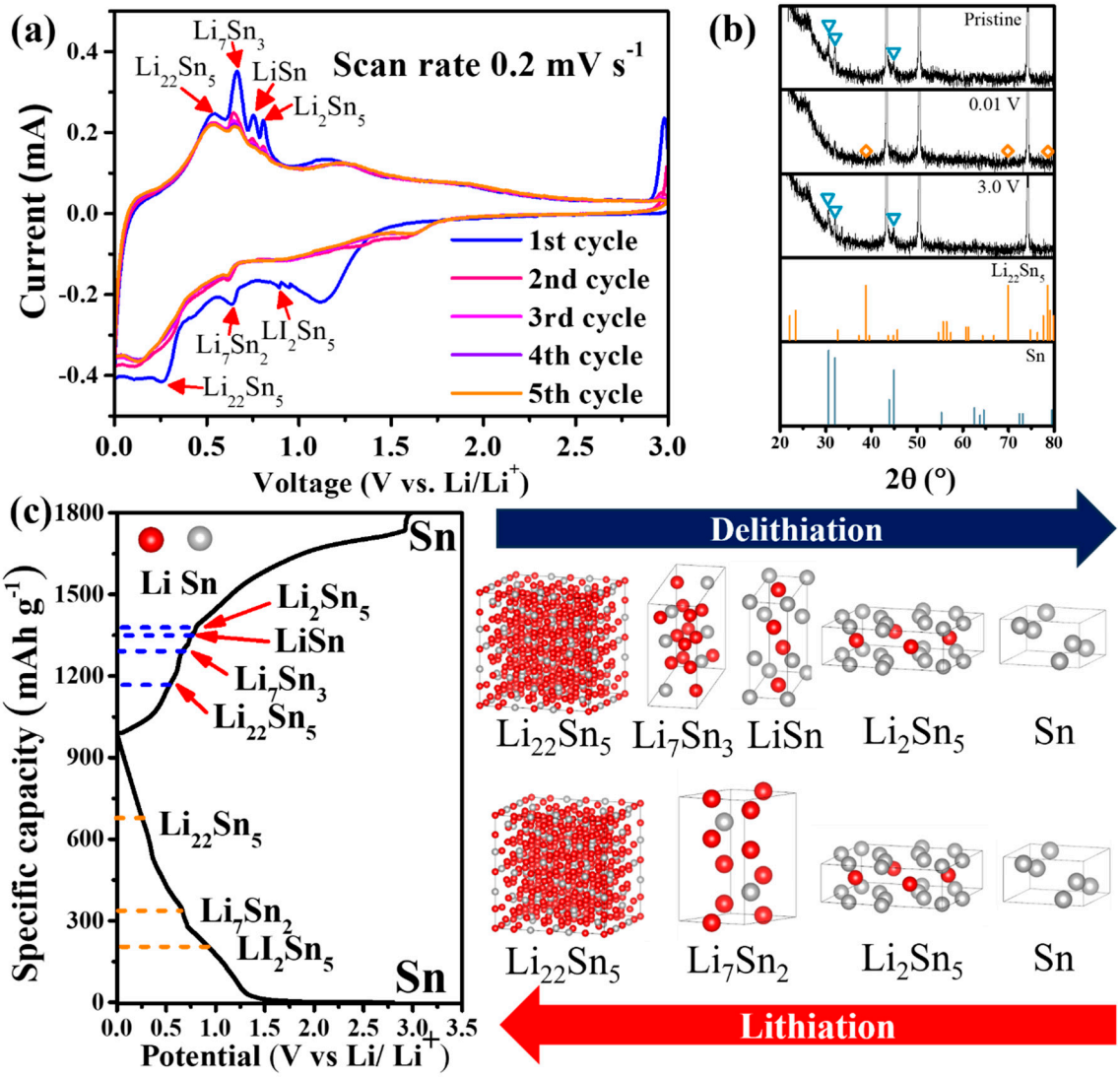

Figure 3. (a) CV results; (b) ex situ XRD (before cycling and at 0.01 and 3 V) results; (c) voltage profile and crystalline phase evolution of Sn-TiO_2-C (20 wt%).

Considering these results, the electrochemical reaction mechanism of Sn-TiO_2-C (20 wt%) can be summarized as follows:

Lithiation

$$5Sn + 2Li^+ + 2e^- \rightarrow Li_2Sn_5 \ (\sim 0.89\ V) \qquad (4)$$

Preprints (www.preprints.org) | NOT PEER-REVIEWED | Posted: 21 September 2023 doi:10.20944/preprints202309.1444.v1

$$2Li_2Sn_5 + 31Li^+ + 31e^- \rightarrow 5Li_7Sn_2\ (\sim 0.63\ V) \quad (5)$$

$$5Li_7Sn_2 + 9Li^+ + 9e^- \rightarrow 2Li_{22}Sn_5\ (\sim 0.27\ V) \quad (6)$$

Delithiation

$$3Li_{22}Sn_5 \rightarrow 5Li_7Sn_3 + 31Li^+ + 31e^-\ (\sim 0.66\ V) \quad (7)$$

$$Li_7Sn_3 \rightarrow 3LiSn + 4\ Li^+ + 4e^-\ (\sim 0.75\ V) \quad (8)$$

$$5LiSn \rightarrow Li_2Sn_5 + 3Li^+ + 3e^-\ (\sim 0.81\ V) \quad (9)$$

$$Li_2Sn_5 \rightarrow 5Sn + 2Li^+ + 2e^-\ (\sim 3\ V) \quad (10)$$

Figure 4a shows the CV profiles of Sn-TiO_2-C (20 wt%) at various scan rates (0.2–1.4 mV s^{-1}). To identify the contribution of capacitive and diffusion-controlled reactions, three distinctive peaks in the delithiation process were selected (peak 1: ~0.60 V, peak 2: ~0.7 V, peak 3: ~1.3 V; peak 1 and 2 correspond to delithiation of Li_ySn, peak 3 corresponds to delithiation of Li_xC) were selected.[36] From the log i (current) vs. log ν (scan rate) plot (**Figure 4b**), the slope *b* was obtained via linear fitting of the following equation:[37]

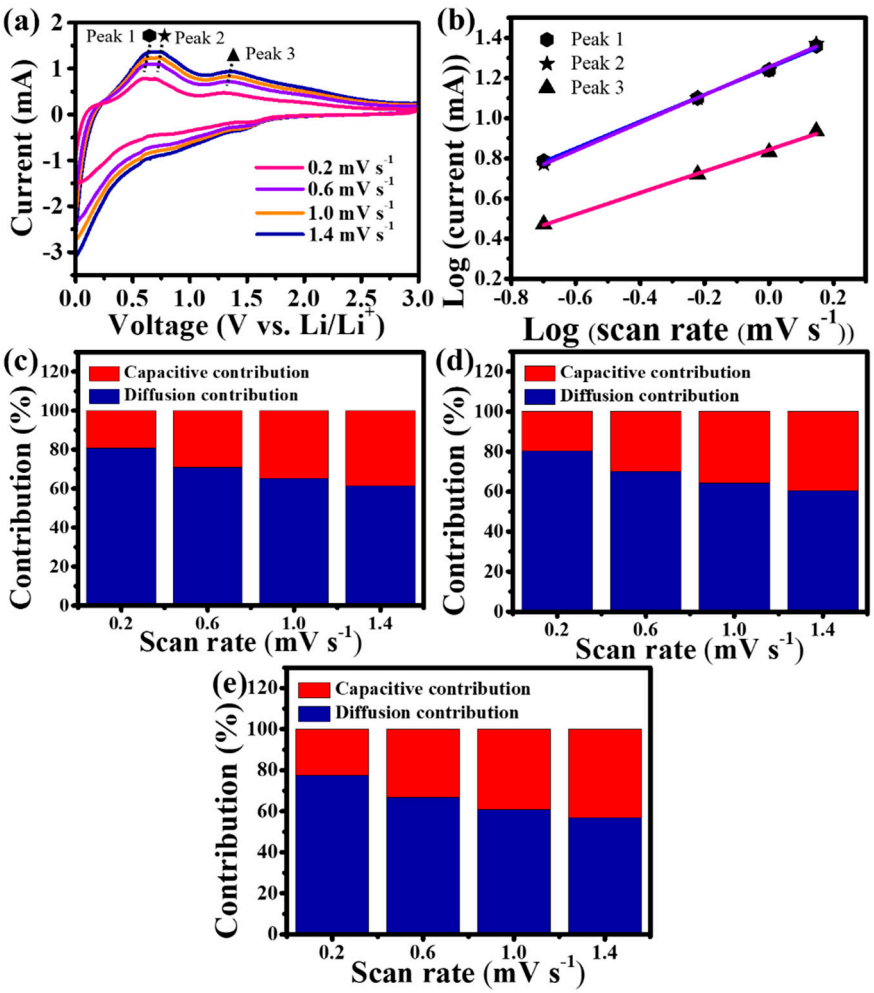

Figure 4. (a) CV of Sn-TiO_2-C (20 wt%) at various scan rates; (b) fitted plot of the current variation with respect to the scan rate; proportions of capacitive and diffusion storage contributions at (c) peak 1, (d) peak 2, and (e) peak 3.

$$\log i = b \log v + \log a \qquad (11)$$

where b values of 1 and 0.5, reflect surface capacitive and diffusion-controlled systems, respectively. The quantitative contributions of the capacitive and diffusion-controlled reactions can be calculated by linearly fitting the $i\, v^{-1/2}$ vs. $v^{1/2}$ plot using the following equation[38, 39]:

$$i\ v^{-1/2} = k_1\, v^{1/2} + k_2 \qquad (12)$$

where k_1 and k_2 are parameters corresponding to the capacitive and diffusion-controlled behaviors, respectively. As shown in **Figures 4c–e**, the contribution from capacitive storage (red bars in the graphs) consistently increased with an increase in the scan rate, regardless of the peak type. This is because the number of Li ions that can diffuse into the internal electrode is reduced at high voltage scan rates, reducing the overall capacity. However, the presence of a capacitive reaction allows fast Li-ion charge-transfer kinetics, enhancing the rate performance. For peaks 1–3, the contributions from the capacitive and diffusion-controlled reactions were 19.22%/80.78%, 19.80%/80.20%, and 22.33%/77.67%, respectively, at a scan rate of 0.2 mV s^{-1}. The appropriate capacitive and diffusion-controlled behavior of Sn-TiO_2-C (20 wt%) was expected to balance the electrochemical kinetics and overall capacity.

3.3. Electrochemical performance of Sn-TiO_2-C anode

Figure 5a presents the cycling performance of Sn-TiO_2-C (20 wt%) in comparison with that of its counterparts (Sn-TiO_2 and Sn-C (20 wt%)) measured at a current density of 200 mA g^{-1}. In the first cycle, Sn-C (20 wt%) exhibited a higher specific capacity (998 mAh g^{-1}) than Sn-TiO_2-C (20 wt%) (990 mAh g^{-1}) and Sn-TiO_2 (628 mAh g^{-1}). This is reasonable considering the theoretical capacities of the samples (Sn-TiO_2-C (20 wt%):657 mAh g^{-1}, Sn-TiO_2:728 mAh g^{-1}, Sn-C (20 wt%):869 mAh g^{-1}) (**Table S1**). The specific capacities of the samples exceeded their theoretical capacities in the first cycle owing to the additional capacity contribution from the SEI layer. As the number of cycles increased, the capacity variation tended to change significantly among the samples. The capacity decreased with an increasing number of cycles for Sn-C (20 wt%), whereas it was stably maintained for Sn-TiO_2-C (20 wt%), except for some capacity drop during the initial several cycles. After 100 cycles, the specific reversible discharge capacity of Sn-TiO_2-C (20 wt%) was 669 mAh g^{-1}, which was significantly higher than that of Sn-C (20 wt%) (247 mAh g^{-1}). For Sn-TiO_2, the capacity rapidly decreased in the first 10 cycles because of the absence of a buffering C matrix. Rate capability measurements revealed a similar trend (**Figure 5b**). Sn-C (20 wt%) exhibited a higher capacity than Sn-TiO_2-C (20 wt%) and Sn-TiO_2 at 0.1 A g^{-1}, as it had the highest theoretical capacity. However, when a higher current density was applied, Sn-TiO_2-C (20 wt%) exhibited superior performance to the other samples, owing to its efficient and stable Li-ion transport. The average discharge capacities of Sn-TiO_2-C (20 wt%) were 586, 563, 540, and 439 mAh g^{-1} at 0.1, 0.5, 1.0, and 3.0 A g^{-1}, respectively. After the original current density recovered to 0.1 A g^{-1}, the capacity retention of Sn-TiO_2-C (20 wt%) was as high as 96%, indicating the reversible and resilient rate performance. **Figure 5c** shows the cycling performance of Sn-TiO_2-C with respect to the C content (10, 20, and 30 wt%). Although Sn-TiO_2-C (20 wt%) and Sn-TiO_2-C (30 wt%) exhibited stable cycling behavior after several initial cycles, Sn-TiO_2-C (10 wt%) exhibited continuous capacity fading owing to the insufficient buffering effect of 10 wt% C in the composite. Sn-TiO_2-C (20 wt%) outperformed Sn-TiO_2-C (30 wt%) because of its higher active Sn content. The reversible specific discharge capacity of Sn-TiO_2-C (20 wt%) was 669 mAh g^{-1} after 100 cycles at 200 mA g^{-1}, which was higher than that of Sn-TiO_2-C (30 wt%) (543 mAh g^{-1}), suggesting that the optimal C content of the Sn-TiO_2-C composite was 20 wt%. Overall, Sn-TiO_2-C (20 wt%) outperformed most recently studied Sn-based anodes for LIBs (**Table S2**). **Figures 5d–f** present the

Preprints (www.preprints.org) | NOT PEER-REVIEWED | Posted: 21 September 2023 doi:10.20944/preprints202309.1444.v1

voltage profiles of Sn-C, Sn-TiO$_2$, and Sn-TiO$_2$-C (20 wt%) from the 1st cycle to the 100th cycle. The initial coulombic efficiencies (CEs) of Sn-C (20 wt%), Sn-TiO$_2$, and Sn-TiO$_2$-C (20 wt%) were 73.5%, 63.5%, and 81.9%, respectively (**Table S3**). As the cycle number increased, the increase in CE was more pronounced for Sn-TiO$_2$-C (20 wt%) than for the other samples. For example, the CE of Sn-TiO$_2$-C (20 wt%) after 10 cycles was 98.3%, which was higher than those of Sn-C (20 wt%) (94.4%) and Sn-TiO$_2$ (96.2%). This indicates the highly reversible lithiation/delithiation of Sn-TiO$_2$-C (20 wt%), which stabilized the cycling performance with an increase in the number of cycles, as shown in **Figures 5a** and **c**. To gain further insight into the good performance of Sn-TiO$_2$-C (20 wt%), EIS was performed. **Figure 5g** shows the Nyquist plots and equivalent circuits (R_{ct}: charge-transfer resistance; R_s: electrolyte resistance; CPE: constant phase element related to the double-layer capacitance; Z_W: Warburg impedance) of Sn-C (20 wt%), Sn-TiO$_2$, and Sn-TiO$_2$-C (20 wt%) in the frequency range of 1–1000 kHz after 20 cycles. From the fitting results (**Table S4**), Sn-TiO$_2$-C (20 wt%) had the smallest R_{ct} value, implying the most efficient charge transport. **Figure 5h** shows the plot of real impedance (Z') vs. $\omega^{-1/2}$ obtained from EIS measurements. The Warburg parameter (σ) was extracted via linear fitting with the following equation:

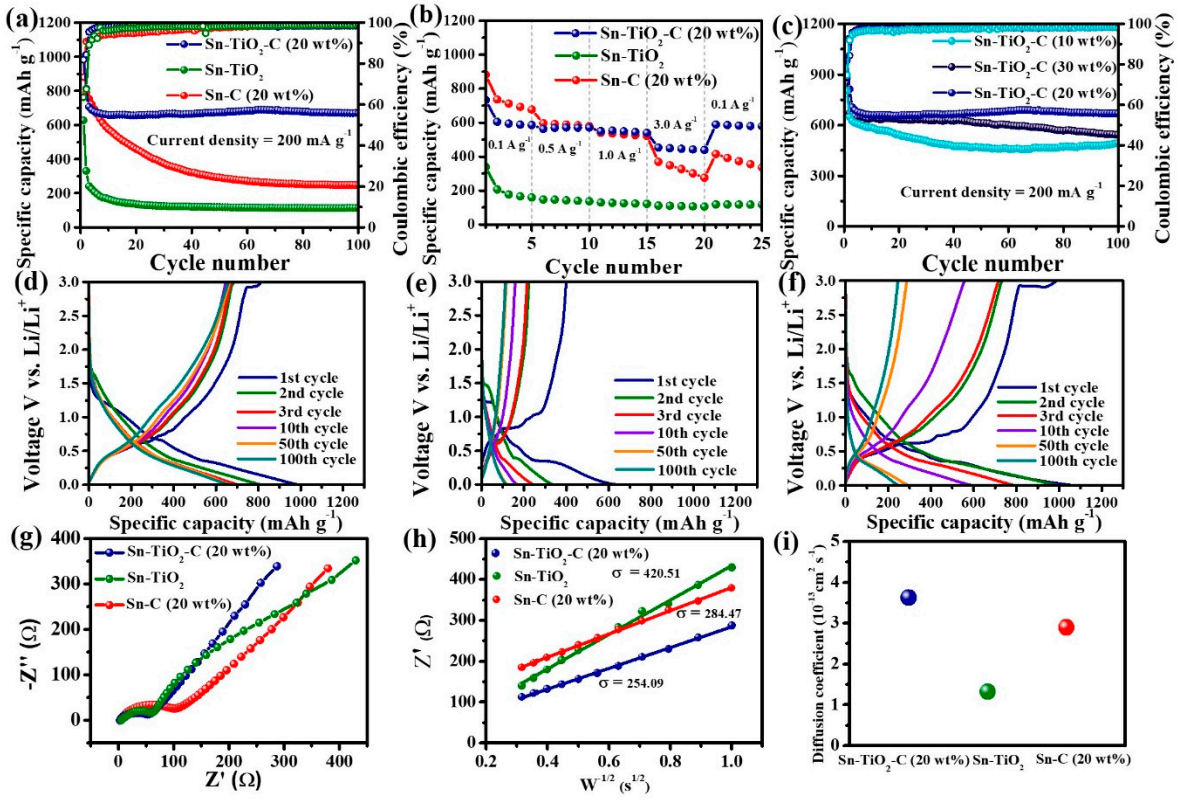

Figure 5. (a) Cycle performance (at 200 mA g^{-1}); (b) rate performance (0.1–3.0 A g^{-1}) of Sn-C (20 wt%), Sn-TiO$_2$, and Sn-TiO$_2$-C (20 wt%); (c) cycle performance of Sn-TiO$_2$-C (10 wt%), Sn-TiO$_2$-C (20 wt%), and Sn-TiO$_2$-C (30 wt%) at 200 mA g^{-1}; voltage profiles of (d) Sn-C (20 wt%), (e) Sn-TiO$_2$, and (f) Sn-TiO$_2$-C (20 wt%) at 200 mA g^{-1}; (g) Nyquist plot and (h) fitting plot of Z' vs. W$^{-1/2}$; (i) diffusion coefficients of Sn-C (20 wt%), Sn-TiO$_2$, and Sn-TiO$_2$-C (20 wt%).

$$Z' = R_s + R_{ct} + \sigma\omega^{-1/2}. \qquad (13)$$

The Li-ion diffusion coefficient (D_{Li+}) can be obtained from the estimated σ via the following equation:

$$D_{Li^+} = \frac{R^2T^2}{2A^2n^4F^4C^2\sigma^2} \qquad (14)$$

where R, T, A, n, F, and C represent the gas constant, absolute temperature, electrode area, number of electrons per molecule (n = 1 mol), Faraday constant, and Li-ion concentration, respectively.

Preprints (www.preprints.org) | NOT PEER-REVIEWED | Posted: 21 September 2023 doi:10.20944/preprints202309.1444.v1

According to the result, the D_{Li+} of Sn-TiO_2-C (20 wt%) was higher (3.6×10^{-13} cm^2 s^{-1}) than those of Sn-C (20 wt%) (2.9×10^{-13} cm^2 s^{-1}) and Sn-TiO_2 (1.3×10^{-13} cm^2 s^{-1}) after 20 cycles, indicating that Sn-TiO_2-C (20 wt%) had a superior Li^+ ion diffusion capability to the other samples (**Figure 5i**).

Figure 6a shows the long-term cycling performance of Sn-based composite electrodes at 500 mA g^{-1}. Similar to the cycling performance measured at a lower current density (200 mA g^{-1}), the Sn-TiO_2-C (20 wt%) electrode exhibited significantly better performance than its counterparts at a high current density (500 mA g^{-1}) during 500 cycles. The reversible specific capacity of Sn-TiO_2-C (20 wt%) was 651 mAh g^{-1} after 500 cycles. For Sn-C (20 wt%), the capacity fading was more severe at this high current density than at a low current density because of the insufficient buffering role of the single C matrix. Notably, the capacity of Sn-TiO_2-C (20 wt%) was gradually increased after approximately 100 cycles, which was likely associated with activation of the electrode and electrolyte decomposition, where more active sites in the electrode were exposed or occupied by Li ions.[40] **Figures 6b–g** present SEM images of Sn-C (20 wt%), Sn-TiO_2-C (20 wt%), and Sn-TiO_2 in the pristine state and after 100 cycles. Although several cracks and large agglomerated particles were observed for Sn-C (20 wt%) and Sn-TiO_2, the morphological change in Sn-TiO_2-C (20 wt%) after cycling was relatively insignificant, indicating the mechanical robustness of Sn-TiO_2-C (20 wt%) supported by the hybrid matrix.

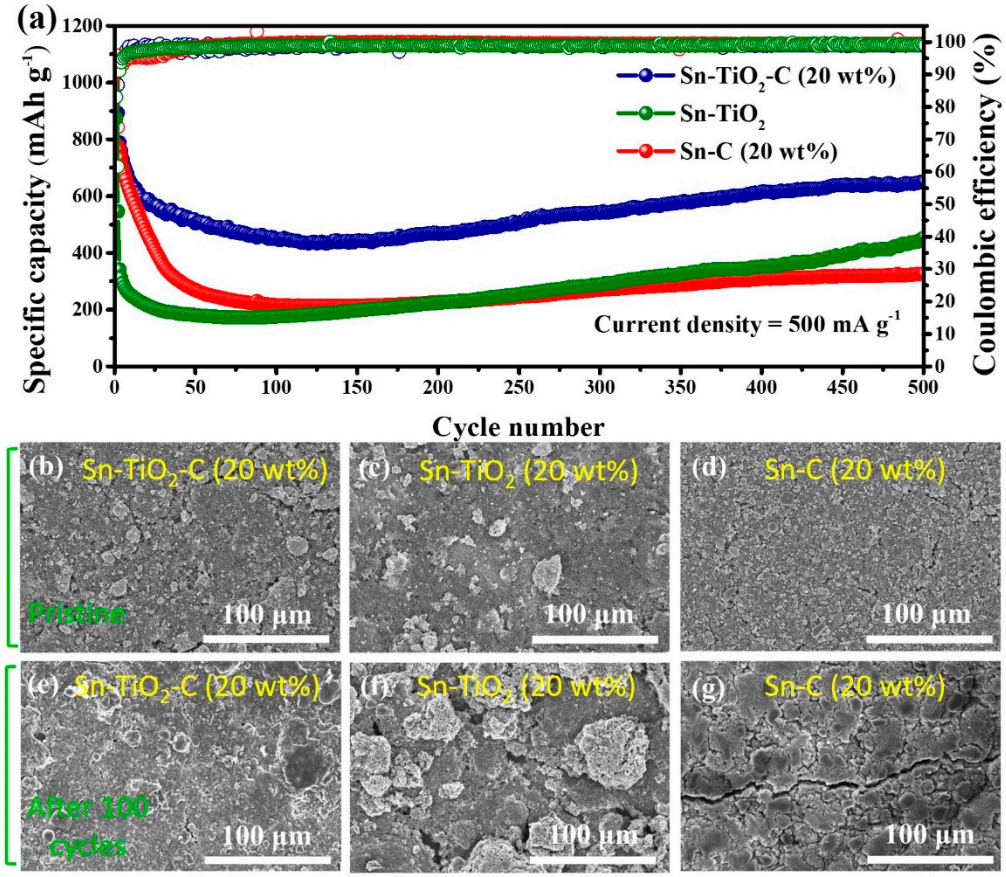

Figure 6. (a) Cycle performance of Sn-TiO_2-C (20 wt%), Sn-TiO_2, and Sn-C (20 wt%) at 500 mA g^{-1}. SEM images of (b, e) Sn-TiO_2-C (20 wt%), (c, f) Sn-TiO_2, (d, g) Sn-C (20 wt%); (b–d) pristine and (e–g) after 100 cycles (applied current density of 500 mA g^{-1}).

4. Conclusion

We developed a ternary Sn-TiO_2-C composite as a potential LIB anode material. XRD, XPS, SEM, TEM, and EDS confirmed the successful synthesis of Sn-TiO_2-C and the homogeneous distribution of its constituents (Sn, TiO_2, and C) without aggregation. Analysis of the electrochemical reaction mechanism revealed that Sn and TiO_2-C were the main active material and supporting matrix,

respectively. The TiO_2-C hybrid matrix synergistically mitigated the volume change of the active Sn during cycling and enhanced the reversible electrochemical reaction. Consequently, Sn-TiO_2-C (20 wt%) delivered 669 mAh g^{-1} (after 100 cycles at 200 mA g^{-1}) and 651 mAh g^{-1} (after 500 cycles at 500 mA g^{-1}), with 99% capacity retention at 200 mA g^{-1} relative to 500 mA g^{-1}. The superiority of Sn-TiO_2-C to Sn-TiO_2 and Sn-C was associated with enhanced Li-ion diffusion properties, as verified by EIS. This study provides valuable insights for the development of high-performance anode materials for LIBs.

Acknowledgments: This work was supported by the Gachon University Research Fund of 2023 (GCU-202304030001) and the Basic Science Research Capacity Enhancement Project through a Korea Basic Science Institute (National Research Facilities and Equipment Center) grant funded by the Ministry of Education (2019R1A6C1010016).

References

1. Kim, S. and K. Park, Electrode design to mitigate the kinetic issue of cathodes in high energy lithium-ion batteries. *J. Power Sources*, **2022**. **547**: p. 231916.
2. Kim, S., S. Na, J. Kim, T.H. Jun, M.H. Oh, K. Min and K. Park, Multifunctional surface modification with Co-free spinel structure on Ni-rich cathode material for improved electrochemical performance. *J. Alloys Compd.*, **2022**. **918**: p. 165454.
3. Cho, H. and K. Park, Mitigating the Kinetic Hindrance of the Poly/Single-Crystalline Ni-Rich Cathode-Based Electrode via Formation of the Superior Electronic/Ionic Pathway. *ACS Appl. Energy Mater.*, **2022**. **5**(9): p. 11223-11228.
4. Na, S. and K. Park, Hybrid dual conductor on Ni-rich NCM for superior electrochemical performance in Lithium-ion batteries. *Int. J. Energy Res.*, **2022**. **46**(6): p. 7389-7398.
5. Tran, M.X., T.-A. Nguyen, J.K. Lee and S.-W. Lee, Porous silicon covalently-grafted with chloro-styrenic carbons for fast Li+ diffusion and durable lithium-storage capability. *J. Power Sources*, **2023**. **554**: p. 232326.
6. Tran, M.X., J.-Y. Woo, T.-A. Nguyen, S.-W. Lee and J.K. Lee, Thermolytically grafted silicon particles with ultrathin carbonaceous coating rich of phenyl moieties as lithium-storage anode material. *J. Chem. Eng.*, **2020**. **395**: p. 125169.
7. Lim, Y.E., W.S. Choi, J.H. Kim, Y.N. Ahn and I.T. Kim, The Sn–red P–Fe–based alloy materials for efficient Li–ion battery anodes. *J. Ind. Eng. Chem.*, **2023**. **121**: p. 299-311.
8. Lee, J., W.S. Jung and S.-W. Lee, N-doped ZnC composites with gelatin coating as enhanced lithium-storage anode materials. *J. Mater. Sci.*, **2022**. **57**(48): p. 21996-22005.
9. Salunkhe, T.T., R.S. Varma, A.N. Kadam, S.-W. Lee, Y.-C. Lee, J. Hur and I.T. Kim, Scraps to superior anodes for Li-ion batteries: Sustainable and scalable upgrading of waste rust. *J. Hazard. Mater.*, **2021**. **410**: p. 124571.
10. Nguyen, Q.H., V.D. Phung, W.G. Kidanu, Y.N. Ahn, T.L. Nguyen and I.T. Kim, Carbon-free Cu/SbxOy/Sb nanocomposites with yolk-shell and hollow structures as high-performance anodes for lithium-ion storage. *J. Alloys Compd.*, **2021**. **878**: p. 160447.
11. Lee, H., A.N. Preman, T.N. Vo, J.H. Lee, I.T. Kim and S.k. Ahn, In situ crosslinkable acrylic random copolymer binders for silicon anodes in lithium-ion batteries. *Int. J. Energy Res.*, **2022**. **46**(9): p. 12565-12578.
12. Inaba, M., T. Uno and A. Tasaka, Irreversible capacity of electrodeposited Sn thin film anode. *J. Power Sources*, **2005**. **146**(1-2): p. 473-477.
13. Sun, J., G. Zheng, H.-W. Lee, N. Liu, H. Wang, H. Yao, W. Yang, et al., Formation of stable phosphorus–carbon bond for enhanced performance in black phosphorus nanoparticle–graphite composite battery anodes. *Nano Lett.*, **2014**. **14**(8): p. 4573-4580.
14. Jin, Y., B. Zhu, Z. Lu, N. Liu and J. Zhu, Challenges and recent progress in the development of Si anodes for lithium-ion battery. *Adv. Energy Mater.*, **2017**. **7**(23): p. 1700715.
15. Qin, J., C. He, N. Zhao, Z. Wang, C. Shi, E.-Z. Liu and J. Li, Graphene networks anchored with Sn@ graphene as lithium ion battery anode. *ACS nano*, **2014**. **8**(2): p. 1728-1738.
16. Bogart, T.D., A.M. Chockla and B.A. Korgel, High capacity lithium ion battery anodes of silicon and germanium. *Curr. Opin. Chem. Eng.*, **2013**. **2**(3): p. 286-293.
17. Idota, Y., T. Kubota, A. Matsufuji, Y. Maekawa and T. Miyasaka, Tin-based amorphous oxide: a high-capacity lithium-ion-storage material. *Science*, **1997**. **276**(5317): p. 1395-1397.
18. Dang, H.X., K.C. Klavetter, M.L. Meyerson, A. Heller and C.B. Mullins, Tin microparticles for a lithium ion battery anode with enhanced cycling stability and efficiency derived from Se-doping. *J. Mater. Chem. A*, **2015**. **3**(25): p. 13500-13506.
19. Hassoun, J., G. Derrien, S. Panero and B. Scrosati, A nanostructured Sn–C composite lithium battery electrode with unique stability and high electrochemical performance. *Adv. Mater.*, **2008**. **20**(16): p. 3169-3175.

20. Fan, X.-Y., F.-S. Ke, G.-Z. Wei, L. Huang and S.-G. Sun, Sn–Co alloy anode using porous Cu as current collector for lithium ion battery. *J. Alloys Compd.*, **2009**. **476**(1-2): p. 70-73.
21. Wu, M., C. Wang, J. Chen, F. Wang and B. Yi, Sn/carbon nanotube composite anode with improved cycle performance for lithium-ion battery. *Ionics*, **2013**. **19**: p. 1341-1347.
22. Fang, L. and B. Chowdari, Sn–Ca amorphous alloy as anode for lithium ion battery. *J. Power Sources*, **2001**. **97**: p. 181-184.
23. Deng, Q., Z. Huang, X. Dai, Y. Wang, Z. Li and J. Li, Three-dimensional nanoporous and nanopillar composite Cu-Sn electrode for lithium-ion battery. *J. Solid State Electrochem.*, **2015**. **19**: p. 1765-1771.
24. Lu, M., Y. Tian, Y. Li, W. Li, X. Zheng and B. Huang, Synthesis and characterization of spherical-like tin-nickel alloy as anode for lithium ion batteries. *Int. J. Electrochem. Sci.*, **2012**. **7**(1): p. 760-767.
25. Hassoun, J., G. Derrien, S. Panero and B. Scrosati, A SnSb–C nanocomposite as high performance electrode for lithium ion batteries. *Electrochim. Acta*, **2009**. **54**(19): p. 4441-4444.
26. Youn, D.H., S.K. Stauffer, P. Xiao, H. Park, Y. Nam, A. Dolocan, G. Henkelman, et al., Simple synthesis of nanocrystalline tin sulfide/N-doped reduced graphene oxide composites as lithium ion battery anodes. *ACS nano*, **2016**. **10**(12): p. 10778-10788.
27. Kim, S.-O. and A. Manthiram, High-performance Zn–TiC–C nanocomposite alloy anode with exceptional cycle life for lithium-ion batteries. *ACS Appl. Mater. Interfaces*, **2015**. **7**(27): p. 14801-14807.
28. Kim, W.S., T.N. Vo and I.T. Kim, GeTe-TiC-C composite anodes for li-ion storage. *Mater.*, **2020**. **13**(19): p. 4222.
29. Kim, I.T., E. Allcorn and A. Manthiram, Cu6Sn5–TiC–C nanocomposite anodes for high-performance sodium-ion batteries. *J. Power Sources*, **2015**. **281**: p. 11-17.
30. Xu, W., L. Kong, H. Huang, M. Zhong, Y. Liu and X.-H. Bu, Sn nanocrystals embedded in porous TiO 2/C with improved capacity for sodium-ion batteries. *Inorg. Chem. Front.*, **2019**. **6**(10): p. 2675-2681.
31. Zhang, S., Y. Xing, T. Jiang, Z. Du, F. Li, L. He and W. Liu, A three-dimensional tin-coated nanoporous copper for lithium-ion battery anodes. *J. Power Sources*, **2011**. **196**(16): p. 6915-6919.
32. Luo, B., T. Qiu, D. Ye, L. Wang and L. Zhi, Tin nanoparticles encapsulated in graphene backboned carbonaceous foams as high-performance anodes for lithium-ion and sodium-ion storage. *Nano Energy*, **2016**. **22**: p. 232-240.
33. Liu, K., J.-a. Wang, H. Zheng, S. Guo, X. Wang, J. Man, X. Wang, et al., A sustainable strategy for fabricating porous carbon supported Sn submicron spheres by self-generated Na 2 CO 3 as templates for lithium-ion battery anode. *Green Chem.*, **2021**. **23**(17): p. 6490-6500.
34. Ren, R., Z. Yang and L. Shaw, Polymorphic transformation and powder characteristics of TiO2 during high energy milling. *J. Mater. Sci.*, **2000**. **35**: p. 6015-6026.
35. Park, J.-W. and C.-M. Park, A fundamental understanding of Li insertion/extraction behaviors in SnO and SnO2. *J. Electrochem. Soc.*, **2015**. **162**(14): p. A2811.
36. Lee, J.H., S.H. Oh, S.Y. Jeong, Y.C. Kang and J.S. Cho, Rattle-type porous Sn/C composite fibers with uniformly distributed nanovoids containing metallic Sn nanoparticles for high-performance anode materials in lithium-ion batteries. *Nanoscale*, **2018**. **10**(45): p. 21483-21491.
37. Tang, K., X. Yu, J. Sun, H. Li and X. Huang, Kinetic analysis on LiFePO4 thin films by CV, GITT, and EIS. *Electrochim. Acta*, **2011**. **56**(13): p. 4869-4875.
38. Wang, H., C. Wang, C. Li and Q. Sun, Wrinkled carbon-coated NiCo2O4 nanoclusters constructed by self-encapsulation of cellulose nanonetwork for lithium-ion batteries. *ACS Sustain. Chem. Eng.*, **2019**. **7**(12): p. 10840-10846.
39. Zhang, Y., Y. Qi, Z. Yin, H. Wang, B. He, X. Liang, J. Li, et al., Nano-V2O5/Ti porous membrane electrode with enhanced electrochemical activity for the high-efficiency oxidation of cyclohexane. *Green Chem.*, **2018**. **20**(17): p. 3944-3953.
40. Ge, P., H. Hou, C.E. Banks, C.W. Foster, S. Li, Y. Zhang, J. He, et al., Binding MoSe2 with carbon constrained in carbonous nanosphere towards high-capacity and ultrafast Li/Na-ion storage. *Energy Stor. Mater.*, **2018**. **12**: p. 310-323.